SAJSET
ISSN: 2992-3581

Savannah Journal of Science and Engineering Technology
Volume: 03; Special Issue: 06; Pages: 533-543; 2025.
www.sajsetjournal.com.ng
DOI: xx.xxxx.x/sajset-03-2025-0075

SAJSET
ISSN: 2992-3581

Assessment of geothermal renewable energy potential of chad basin using aeroradiometric and remote sensin techniques

[1]Ogah, A. J. and [2]Mustapha, B. A.
[1]Centre for Atmospheric Research, National Space Research and Development Agency, Prince Abubakar Audu University Campus, Anyigba, Kogi State, Nigeria
[2]Zonal Advanced Space Technology Applications Laboratory, National Space Research and Development Agency, Bayero University Campus, Kano State, Nigeria
ogah.aj@carnasrda.com; mustaphababa625@gmail.com

Paper History
Received: 01st October, 2025
Accepted: 15th October, 2025
Published: October, 2025

Corresponding author
Ogah, A. J.
ogah.aj@carnasrda.com

Abstract:
Geothermal energy is an increasingly attractive renewable energy source, especially for regions facing high energy demand and climate change challenges. This study assesses the geothermal potential of the Chad Basin, northeast Nigeria, by integrating Aeroradiometric and remote sensing techniques. Aeroradiometric datasets, including uranium, thorium, potassium (K^{40}), and total count radiations, were analysed to quantify radiogenic heat production (RHP), while remote sensing techniques were employed to map lineaments, hydrothermal alteration, land surface temperature (LST), and emissivity. The results show a distinct northwest–southeast trend in radioelement distribution, with uranium, thorium, and potassium (K^{40}) enrichment concentrated in the southeastern corridor, where RHP reaches up to 53.1 μW/m³. Remote sensing further revealed structurally controlled thermal anomalies in Mafa, Ajiri, and Asula Fura, correlating with zones of hydrothermal alteration and high LST. Comparison with previous geothermal studies, including bottom-hole temperature (BHT) gradients (~37.5 °C/km) and Curie point depths (18–25 km), confirms the southeastern Chad Basin as the most prospective geothermal target. This integrated approach demonstrates that geothermal potential in the basin is controlled by both radiogenic enrichment and tectonic structures, offering a robust framework for renewable energy exploration in underexplored frontier basins.

Keywords: Geothermal, Remote Sensing, Renewable Energy

1. Introduction

The growing global energy demand, coupled with the urgent need to reduce greenhouse gas emissions, has intensified the search for sustainable and renewable energy resources. Among these alternatives, geothermal energy has emerged as a reliable and environmentally friendly option due to its vast potential for base-load electricity generation and direct-use applications. For countries such as Nigeria, where dependence on fossil fuels remains high, geothermal resources offer a promising pathway for diversifying the energy mix and improving energy security (Bertani, 2016; DiPippo, 2021).

Recent advances in geoscience methods, including Aero-radiometric and remote sensing techniques, have significantly improved geothermal resource assessment. Aero-radiometric data sets provide insight into the spatial distribution of radiogenic heat-producing elements such as uranium (U), thorium (Th), and potassium (K^{40}), which are crucial contributors to geothermal systems (Ali and Orazulike, 2010; Lawal, *et al.,* 2017). Similarly, remote sensing techniques, particularly thermal infrared and lineament analysis, are increasingly used to identify surface geothermal manifestations, structural corridors, and hydrothermal alteration zones (Pour and Hashim, 2015; Yalcin, 2021; Wubalem and Solomon, 2023). The integration of these methods enables a comprehensive understanding of both subsurface radiogenic sources and surface geothermal indicators.

Despite these advancements, geothermal studies in the Chad Basin have largely focused on aeromagnetic and bottom-hole temperature (BHT) data, which, while valuable, provide limited insight into radiogenic heat contribution and surface thermal manifestations (Tyoh et al., 2021; Abdullahi et al., 2022). The lack of integrated studies that combine aeroradiometric analysis with remote sensing limits our understanding of how crustal radiogenic enrichment and structural controls interact to localize geothermal potential. Consequently, geothermal exploration in northeast Nigeria remains underdeveloped, with little progress toward practical utilization (Egwumah, *et al.,* 2020; Nwankwo, 2021).

Various previous studies have provided important baselines. A few of these include that of Tyoh et al. (2021) that reported geothermal gradients of ~37.5 °C/km from BHT data in the Bornu Basin, while Lawal, *et al.* (2017) estimated Curie point depths of 18–25 km and heat flow of

63–95 mW/m² from aeromagnetic interpretation. Similarly, studies by Fairhead (1986), Obaje (2009), and more recently, Abdullahi, *et al.* (2022), highlighted the structural and tectonic framework of the Chad Basin as a key factor influencing heat flow distribution. However, these studies did not fully account for the role of radiogenic heat production from U, Th, and K^{40} anomalies or surface indicators detectable by satellite data, leaving a critical knowledge gap in geothermal assessment.

The aim of this study is to assess the geothermal renewable energy potential of the Chad Basin, northeast Nigeria, by integrating Aeroradiometric and remote sensing techniques. Specifically, the study seeks to (i) map the distribution of uranium, thorium, and potassium (K^{40}) and estimate radiogenic heat production; (ii) analyse lineament density, hydrothermal alteration, and surface thermal anomalies from remote sensing; and (iii) correlate these results with previous geothermal studies to provide a comprehensive evaluation of geothermal prospects of the basin.

2. Methodology

2.1 Location map of the study area

Figures 1 and 2 depict the location and geological setting of the study area which is situated in Chad Basin region of northeastern Nigeria. The inset map of Nigeria highlights the position of the study area within the broader national framework. Geographically, the area is bounded between latitudes 12°00'N–12°30'N and longitudes 13°00'E–13°30'E, and encompasses several Local Government Areas in Borno State of North-Eastern Nigeria.

2.2 Geology map

Geologically, the study area lies within the Quaternary sediments of the Chad Basin, which represent the youngest depositional sequence in the basin (Carter et al., 1963; Barber, 1965). These deposits consist predominantly of unconsolidated sand, silt, clay, and alluvium, which overlie the older Cretaceous to Tertiary formations (Avbovbo et al., 1986; Obaje, 2009). The Quaternary sediments are of significant hydrogeological and environmental importance, as they form the main shallow aquifers that sustain local water supply and agricultural activities (Offodile, 1992; Ngah and Abubakar, 2018).

This spatial framework, which integrates administrative boundaries, road networks, town points, and geological units, provides an essential baseline for further geophysical and remote sensing investigations aimed at delineating subsurface structures, assessing mineralization potential, and evaluating groundwater resources in the Chad Basin.

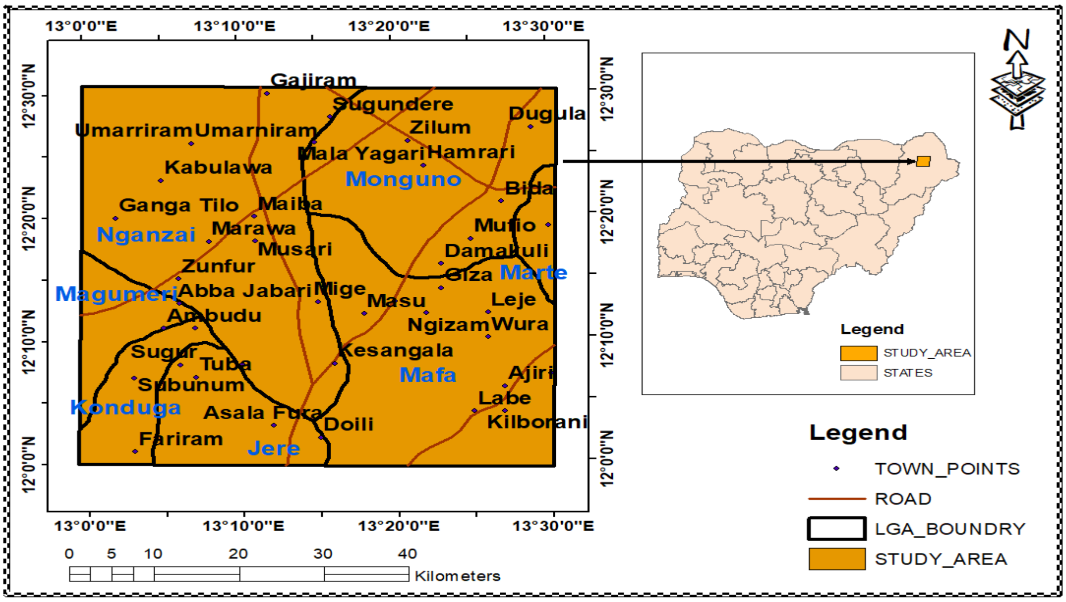

Figure 1: Location map of the study area

2.3 Theoretical background

2.3.1 Radiometric method (Radiogenic heat production)

Radiogenic heat production (RHP) was estimated from Aeroradiometric concentrations of U, Th, and K^{40} using the analytical approach of Rybach (1976) and Salem and Fairhead (2011). This method derives heat generation from radioactive decay processes, reflecting the contribution of basement rocks and soils in the radiogenic heat production given equation 1

$$RHP\ (\mu W/m^3) = \rho(0.0952\, C_u + 0.0256\, C_{Th} + 0.0348\, C_k) \quad (1)$$

Where ρ\rho represents the rock density in kg/m³, C_u, C_{Th}, and C_k denote the concentrations of Uranium (in ppm), Thorium (in ppm), and Potassium (K^{40}, in %), respectively.

This equation integrates the radiogenic contributions from these three major heat-producing elements to determine the total heat output per unit volume of rock.

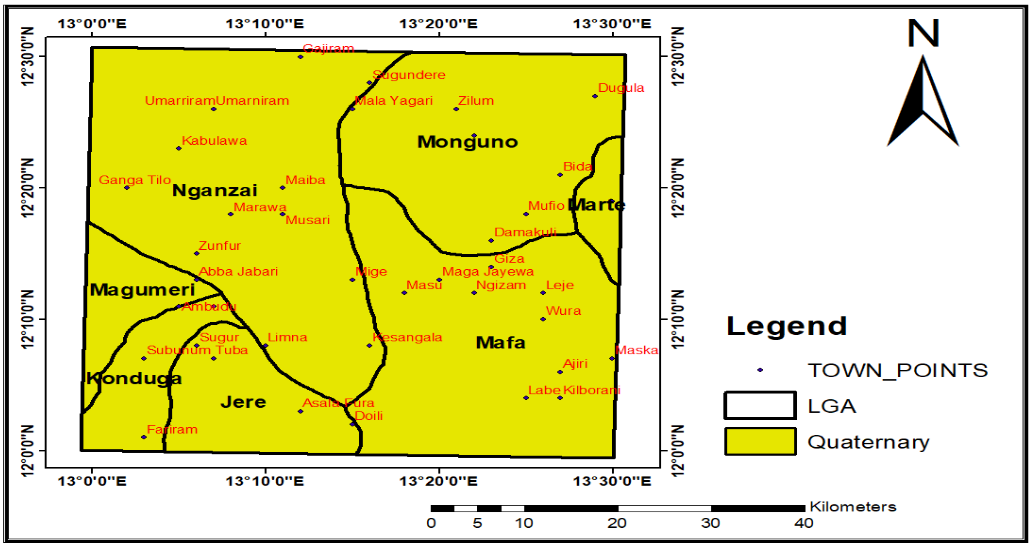

Figure 2: Geology map of the study area (NGSA2010)g

2.3.2 Remote sensing method

2.3.2.1 Thermal surface structural mapping

Step 1: Obtain Satellite Data

Use TIR bands from satellite sensors such as: Landsat 8/9: Band 10 (10.6–11.19 μm)

Step 2: Convert Digital Number (DN) to Top of Atmosphere (TOA) Spectral Radiance using equation 2:

$$L\lambda = ML \times Qcal + AL \quad (2)$$

Where Lλ: TOA spectral radiance (W/m²·sr·μm), ML: Radiance multiplicative scaling factor (from metadata), AL: Radiance additive scaling factor (from metadata) and Qcal: Quantized calibrated pixel value (DN)

Step 3: Convert TOA Radiance to Brightness Temperature (BT). The metadata attached to Landsat 8 scene contains the constant thermal values. These values are used to convert spectral radiance to the BT from Kelvin (K)

$$TB = \frac{K_2}{Ln(K_1/L\lambda + 1)} \quad (3)$$

Where TB: Brightness Temperature in Kelvin, K1, K2: Thermal conversion constants (from metadata) and Lλ: TOA spectral radiance

Step 4: Calculate NDVI for Emissivity Correction. Calculate Normalized Difference Vegetation Index NDVI is a standard vegetation index used to estimate the vegetation health and can be calculated using the Near-infrared (band 5) and Red (band 4) bands. It is expressed as in equation (4):

$$NDVI = \frac{(Band5 - Band4)}{(Band5 + Band4)} \quad (4)$$

For Landsat 8/9:

Where Red = Band 4 and NIR = Band 5

Step 5: Estimate Proportion of Vegetation (PV). Calculating Land Surface Emissivity E accounts for the mean emissivity of a component on the earth surface. It is calculated from the NDVI. Before calculating the E, the Proportion of Vegetation (PV) is premeditated first, as shown in equation 5:

$$Pv = \left(\frac{NDVI - NDVImin}{NDVImax - NDVImin}\right)^2 \quad (5)$$

Where NDVImin, NDVImax: Minimum and maximum NDVI

Step 6: Calculate Surface Emissivity (ε)**.** This was calculated using equation 6:

$$\varepsilon = 0.004 \times Pv + 0.986 \quad (6)$$

Or use land cover-specific values as needed.

Step 7: Calculate Land Surface Temperature (LST)**:** Finally, to calculate the LST, equation 7 is used

$$LST = \frac{TB}{[1 + (\lambda \times TB / \rho) \times \ln(\varepsilon)]} \quad (7)$$

Where LST: Land Surface Temperature in Kelvin, TB: Brightness temperature (K), λ: Wavelength of emitted radiance (~10.895 μm for Landsat 9 Band 10), ε: Surface emissivity and ρ = h·c / σ = 1.438 × 10^{-2} m·K

2.4 Materials

This study utilized a combination of airborne geophysical and satellite remote sensing datasets. The Aeroradiometric and geological maps covering the Nigerian sector of the Chad Basin were obtained from the Nigerian Geological Survey Agency (NGSA). These datasets provide the spatial distribution of radiogenic heat-producing elements (K, Th, and U) and associated geological features critical for geothermal assessment (Ali and Orazulike, 2010). Multispectral remote sensing data, including Landsat 8 Operational Land Imager (OLI) and Thermal Infrared Sensor (TIRS), were acquired from the United States Geological Survey (USGS) Earth Explorer platform. Additionally, the Advanced Spaceborne Thermal Emission and Reflection Radiometer (ASTER) Digital Elevation Model (DEM) was used for terrain correction, structural analysis, and enhancement of lineament mapping (Pour and Hashim, 2015; Yalcin, 2021).

2.5 Methods

2.5.1 Aeroradiometric data processing

The Aeroradiometric data were processed to extract information on radiogenic elements and radiogenic heat production. Key steps included:

a. **Total Count (TC):** Aggregation of overall radioelement concentration to delineate geochemically enriched zones.
b. **Potassium (K), Thorium (Th), and Uranium (U) concentrations:** Used to estimate the abundance of heat-producing elements.
c. **Radiogenic Heat Production (RHP):** Computed using standard equations that relate concentrations of U, Th, and K to heat generation (Rybach, 1988; Lawal, *et al.,* 2017).

This processing enabled the identification of radiogenic anomalies that may contribute significantly to geothermal energy potential.

2.5.2 Remote Sensing Data Processing

To characterize surface manifestations of geothermal activity, Landsat 8 and ASTER DEM data were processed using established geospatial techniques:

a. **Lineament Extraction and Density:** Lineaments were automatically and manually mapped from directional filtering and shaded relief images of ASTER DEM. Lineament density analysis were performed to identify structural corridors favourable for fluid flow and geothermal systems (Wubalem and Solomon, 2023).
b. **Hydrothermal Alteration Mapping:** Band ratio and false-color composite techniques were applied to highlight hydrothermal alteration minerals associated with geothermal activity (Pour and Hashim, 2015).
c. **Top-of-Atmosphere (TOA) Reflectance and Brightness Temperature:** Corrected reflectance and thermal data were derived from Landsat 8 OLI and TIRS bands to ensure radiometric accuracy (USGS, 2019).
d. **Normalized Difference Vegetation Index (NDVI) and Proportion of Vegetation (PV):** These vegetation indices were calculated to estimate surface emissivity and minimize land cover interference in thermal analysis (Sobrino, *et al.,* 2004).
e. **Land surface emissivity (LSE) and land surface temperature (LST):** Derived using the NDVI-based emissivity method and split-window algorithm, enabling detection of thermal anomalies that may indicate subsurface geothermal activity (Jiménez-Muñoz, *et al.,* 2014).

2.5.3 Analysis and interpretation of aeroradiometric remote sensing met

The results from Aeroradiometric and remote sensing datasets were integrated to evaluate geothermal potential in the Chad Basin. Radiogenic heat production anomalies were spatially correlated with structural features derived from lineament density maps, hydrothermal alteration zones, and thermal anomalies from LST. This multidisciplinary approach provided a comprehensive assessment of crustal radiogenic heat contribution and surface geothermal indicators, while also enabling comparison with previous geothermal studies based on aeromagnetic and bottom-hole temperature data (Tyoh, *et al.,* 2021; Abdullahi, *et al.,* 2022).

3. Result

3.1 Aeroradiometric Method

3.1.1 Interpretation of Total Count (TC)

The Total Count (TC) Figure 3 of the study area, measured in counts per second (CPS), reflects the natural gamma radiation intensity, which typically indicates the distribution of radioactive elements such as Uranium (U), Thorium (Th), and Potassium (K).

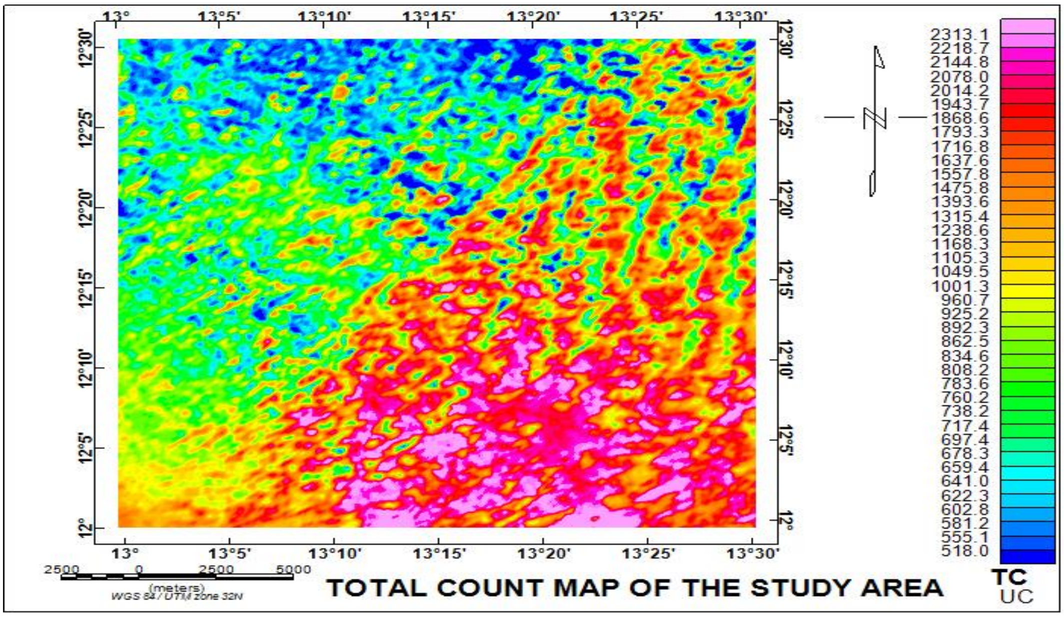

Figure 3: Total Count Map of the Study Area

The values range from 518.0 to 2313.1 CPS.High TC values, illustrated by pink, red, and orange tones, are concentrated predominantly in the south eastern to central regions of the study area. These zones may correspond to felsic and highly altered rocks, often associated with radioelement-rich lithologies or mineralization zones, and may indicate regions of hydrothermal alteration or granitic intrusions. In contrast, low TC values (shown in blue to green shades) dominate the northwestern parts, implying low radiogenic content which may be indicative of mafic, sedimentary, or water-saturated formations.

3.1.2 Thorium Map

The thorium Figure 4 shows a northwest–southeast trending distribution similar to uranium, with high concentrations (>15 ppm) occurring in the central to southern parts of the area between latitudes 12°00'–12°15'N and longitudes 13°05'–13°25'E, while low values (<3 ppm) dominate the northwestern sector. This enrichment in the southern zone indicates higher radiogenic heat production, implying greater geothermal potential compared to the northern part of the study area.

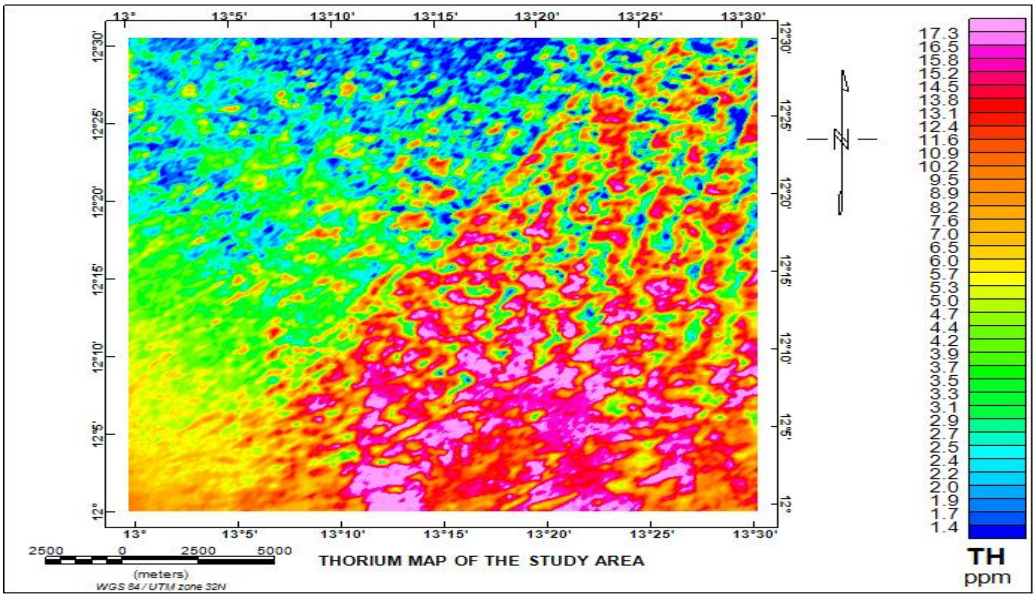

Figure 4: Thorium Map of the Study Area

3.1.3 Potassium map

The potassium Figure 5 shows concentrations ranging from 0.4% to over 1.6%, with a strong northwest–southeast trend similar to uranium and thorium. The highest potassium values, represented in pink to red, are concentrated in the southern part of the area between latitudes 12°00'–12°15'N and longitudes 13°05'–13°25'E, while lower values (<0.6%), shown in blue to cyan, dominate the northwestern sector around 12°20'–12°30'N and 13°00'–13°10'E. Since potassium is also a heat-producing element, its enrichment in the southern sector further enhances radiogenic heat generation and supports the higher geothermal potential already indicated by uranium and thorium maps.

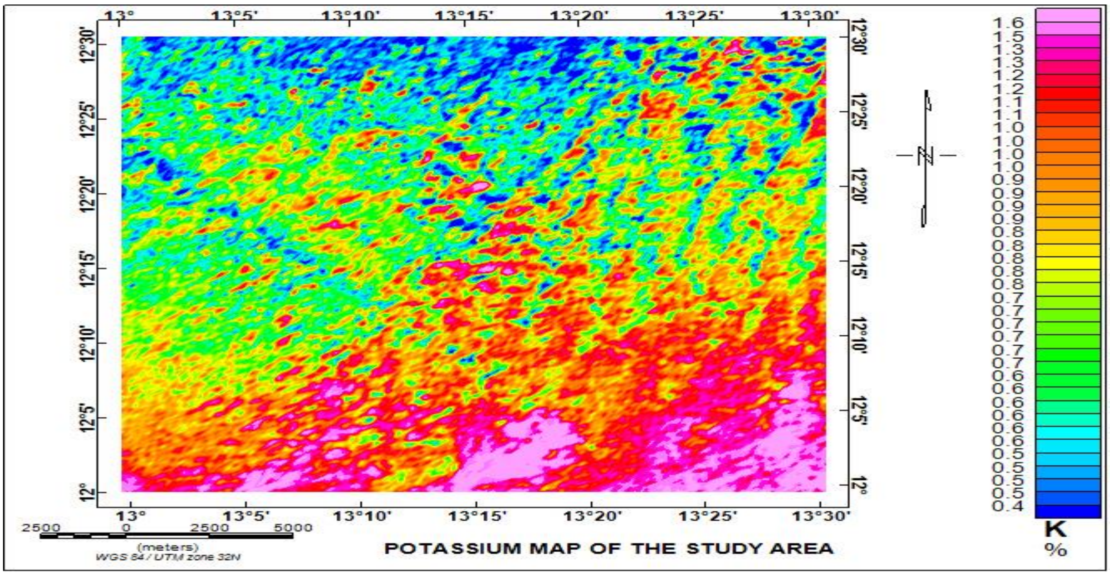

Figure 5: Potassium map of the study area

3.1.4 Uranium map

The uranium Figure 6 shows a clear northwest–southeast trending distribution of anomalies. High uranium concentrations, exceeding 2.0 ppm and represented by pink to red colours, are concentrated between latitudes 12°00'–12°15'N and longitudes 13°05'–13°25'E in the central to southern part of the area.

In contrast, low concentrations (<0.2 ppm), indicated in blue to cyan, dominate the northwestern sector around latitudes 12°20'–12°30'N and longitudes 13°00'–13°10'E. This spatial trend suggests structural control on uranium enrichment and implies that the southern sector has higher geothermal potential due to the abundance of radiogenic heat-producing elements.

3.1.5 Ternary map

The ternary radiometric Figure 7 (12°00'–12°30'N; 13°00'–13°30'E) shows a clear northwest–southeast trend in radioelement distribution. The southeastern sector is enriched in uranium and thorium, indicating felsic basement rocks with high radiogenic heat potential, while the northern and northwestern areas reflect low values typical of sedimentary cover. This spatial pattern highlights the southeastern part as the most prospective zone for geothermal energy exploration.

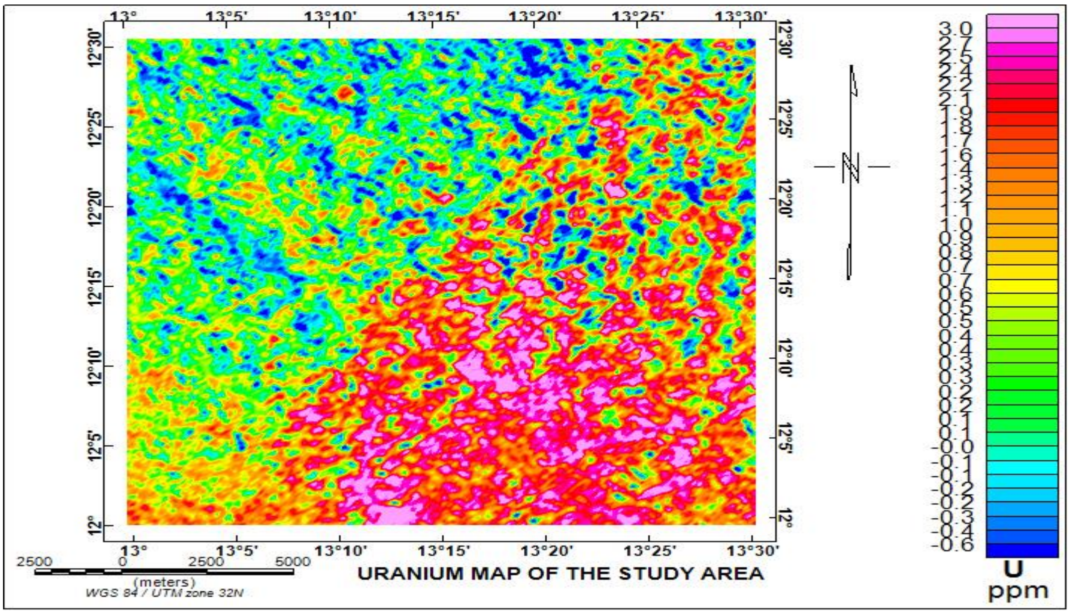

Figure 6: Uranium map of the study area

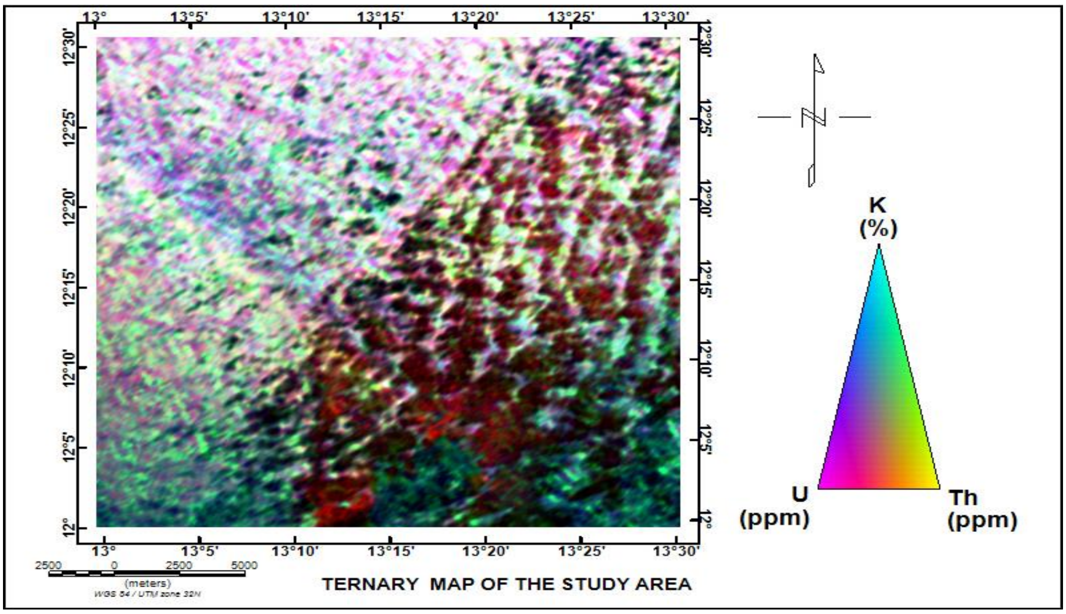

Figure 7: Ternary map of the study area

3.1.6 Radiogenic heat production

The Radiogenic Heat Production (RHP) Figure 8 delineates the spatial variability of heat-generating zones within the study area, with values ranging from 4.1 to 53.1 μW/m³. Color coding highlights this distribution, where low RHP values (4.1–10 μW/m³) appear in blue and green shades, while higher values (>20 µW/m³) are represented by red, pink, and purple tones. The southeastern and south-central sectors exhibit the highest concentrations of radiogenic heat, whereas the northern and northwestern portions display markedly lower values. A general increase in RHP is observed along a northeast–southeast gradient, reflecting variations in subsurface lithology and concentrations of heat-producing elements. The elevated RHP in the southern and southeastern regions suggests enrichment in uranium (U), thorium (Th), and potassium (K), elements that dominate radiogenic heat generation. These anomalies are most likely associated with felsic basement rocks or intrusive bodies that are either exposed or occur at shallow depths.

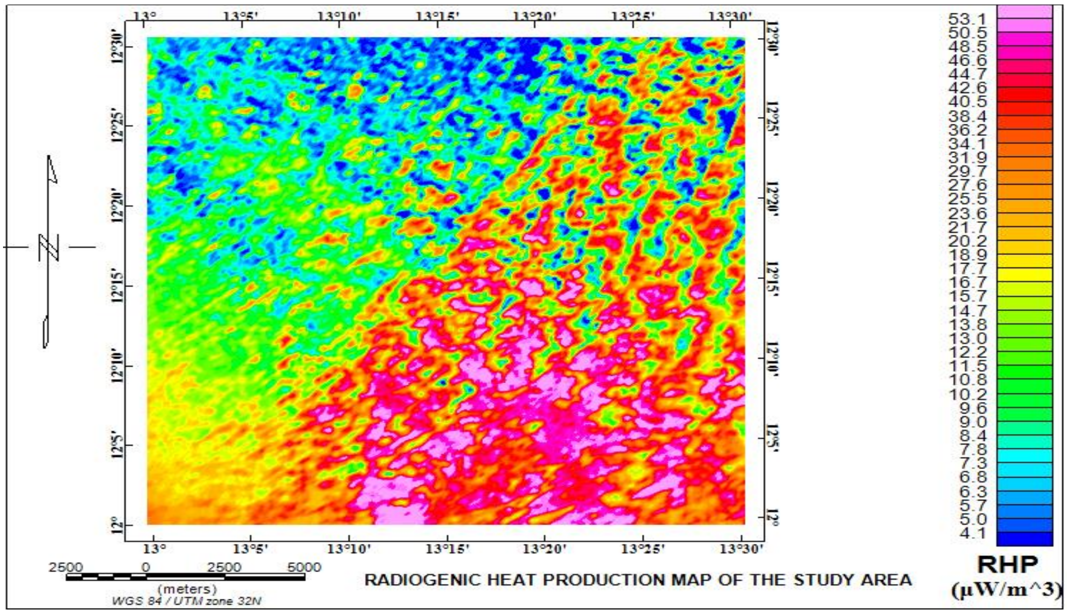

Figure 8: Radiogenic Heat Production Map of the Study Area

3.2 Remote sensing methods

3.2.1 Lineaments

The lineament map (Figure 9a) reveals a dominant NE–SW and NW–SE structural orientation across the study area, with particularly dense concentrations around Nganzai, Ganga Tilo, Mafa, Bufejuma, Konduga, and Asula Fura (12°00'–12°30'N; 13°00'–13°30'E). These linear anisotropic features represent zones of enhanced crustal fracturing that play a crucial role in geothermal systems by providing conduits for deep-seated heat and fluid circulation. Their spatial coincidence with zones of hydrothermal alteration emphasizes their tectonic and geothermal significance in delineating areas of enhanced geothermal potential.

3.2.2 Lineament density

The lineament density distribution (Figure 9b) highlights structurally controlled corridors that may serve as preferential pathways for geothermal fluid migration. Zones of high to very high density follow the NE–SW and NW–SE structural framework, particularly in Nganzai, Ganga Tilo, Mafa, Musari, Abba Jabari, Bufejuma, Konduga, and Asula Fura (12°00'–12°30'N; 13°00'–13°30'E). These structurally deformed belts suggest enhanced subsurface permeability and active heat transfer, marking them as prime targets for geothermal exploration.

3.2.3 Hydrothermal alteration

The hydrothermal alteration map (Figure 9c), derived from Landsat 8 band ratio (6/7), delineates zones of elevated alteration intensity indicative of geothermal activity. Areas such as Mafa, Masu, Kesangala, Labu, and Asula Fura (12°00'–12°30'N; 13°10'–13°30'E) exhibit strong alteration signatures. The observed NE–SW and NW–SE trends confirm the structural control of fault systems in directing hydrothermal circulation. These thermally altered zones represent prospective geothermal targets warranting further detailed geophysical investigation.

3.2.4 Top-of-atmosphere reflectance

The top-of-atmosphere reflectance (Figure 10a) shows marked spatial variability across the basin. Very low reflectance values (dark blue) dominate the southwestern localities such as Konduga, Jere, and Fariram (12°00'–12°10'N; 13°00'–13°10'E). Central regions including Mafa and Kesangala (12°10'–12°20'N; 13°10'–13°20'E) exhibit low to moderate reflectance (light blue to beige), while the northern and northeastern areas (Monguno, Hamrari, Mangal: 12°20'–12°30'N; 13°20'–13°30'E) display high to very high reflectance (orange to red). These variations correspond to differences in surface composition and thermal properties.

3.2.5 Brightness temperature

The brightness temperature distribution (Figure 10b) reveals a southwest–northeast gradient. Southwestern zones (Jere, Konduga) exhibit very low to low brightness values, reflecting vegetative or moisture-rich surfaces. In contrast, the central and northeastern parts, particularly

Mafa and Monguno, register moderate to very high brightness temperatures, potentially signifying geothermal anomalies or exposed lithologies. This spatial gradient is consistent with localized subsurface heat flow and suggests thermally anomalous areas requiring further geophysical validation.

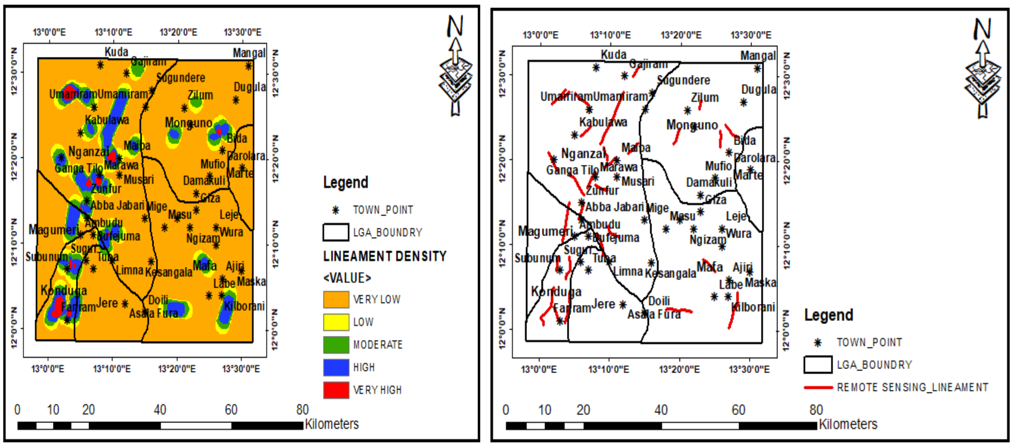

(a) (b)

Figure 9: (a) LD lineament Density (b) Lineament (L)

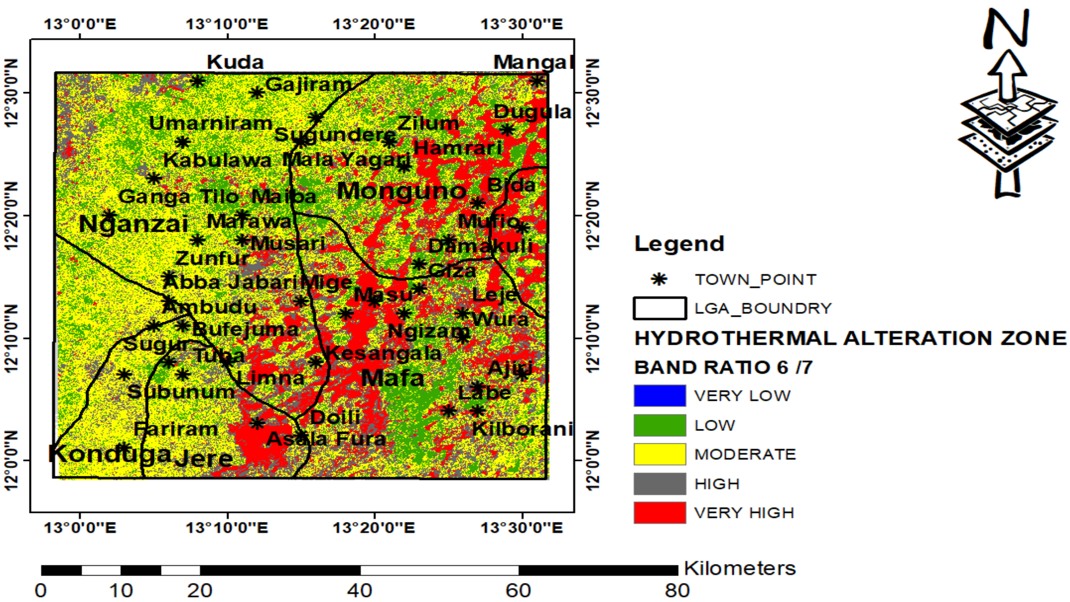

Figure 9: (c) Hydrothermal Map of the study area

3.2.6 Normalized difference vegetation index (NDVI)

The NDVI map (Figure 10c) reflects spatial variations in vegetation density across the basin. Central zones (Mafa, Kesangala, Asula Fura: 12°00'–12°20'N; 13°10'–13°30'E) exhibit very low NDVI values, indicating sparse or degraded vegetation, possibly influenced by elevated land surface temperatures. By contrast, higher NDVI values occur in Konduga, Jere, Nganzai, and Monguno (12°00'–12°30'N; 13°00'–13°10'E), corresponding to healthier vegetation cover. This inverse relationship between vegetation density and thermal anomalies further supports geothermal interpretations.

3.2.7 Proportion of vegetation (PV)

The PV map (Figure 10d) demonstrates significant spatial variability. Very low vegetation cover (blue) dominates the southeastern corridor (Mafa, Asula Fura, Kilborani: 12°00'–12°10'N; 13°20'–13°30'E). Central areas such as Kesangala and Monguno (12°10'–12°20'N; 13°10'–13°20'E) reveal low to moderate values (green to yellow), while the northwestern sector (Kuda, Umarniam, Nganzai: 12°20'–12°30'N; 13°00'–13°10'E) shows high to very high vegetation proportions (red to pink). These patterns correspond to environmental gradients that influence surface thermal dynamics.

3.2.8 Land surface emissivity (LSE)

The LSE distribution (Figure 10e) underscores the thermal heterogeneity of the basin. Very low to low emissivity values (pink to yellow) dominate the southern and southeastern sectors (Doili, Asula Fula, Limna, Mafa, Ajiri, Kilborani: 12°00'–12°20'N; 13°10'–13°30'E). These zones, often associated with exposed lithologies or arid surfaces, suggest potential geothermal anomalies. Moderate to high emissivity values (green to yellow) characterize the northwestern and central localities (Nganzai, Gajiram, Musari, Monguno: 12°10'–12°30'N; 13°00'–13°20'E), reflecting vegetative or soil-moisture-rich terrains indicative of thermally stable conditions.

3.2.9 Land surface temperature (LST)

The LST distribution (Figure 10f) reveals a systematic thermal gradient trending from southwest to northeast. Very high temperature zones (red) are concentrated in the southeastern part of the study area, notably Kilborani, Ajiri, Labe, and parts of Mafa (12°00'–12°15'N; 13°20'–13°30'E), marking potential geothermal hotspots linked to shallow heat sources or fluid circulation. High LST (orange) extends through central Mafa to Monguno (12°10'–12°25'N; 13°10'–13°30'E), aligning with structurally active corridors. Moderate to low LST (yellow to light green) occurs in the central-west and northern sectors (Zilim, Sugundere, Gajiram, Kabuluwa: 12°15'–12°30'N; 13°00'–13°15'E), while very low LST (dark green) dominates the southwestern localities (Konduga, Jere, Farfaram: 12°00'–12°15'N; 13°00'–13°10'E), corresponding to deeper heat sources or thicker sediment cover.

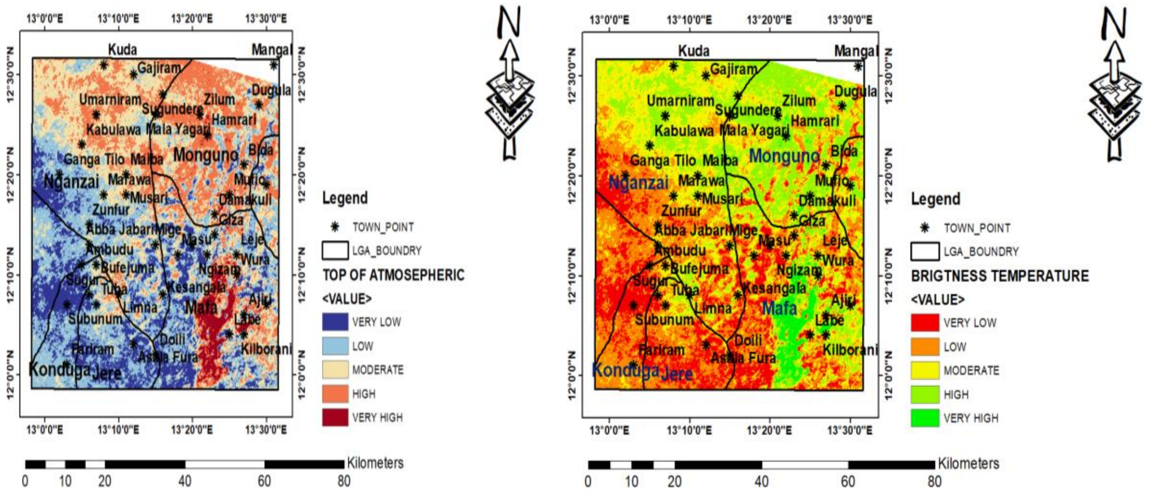

(a) (b)

Figure 10: (a) Top of Atmospheric (b) Brightness Temperature Map of the study area

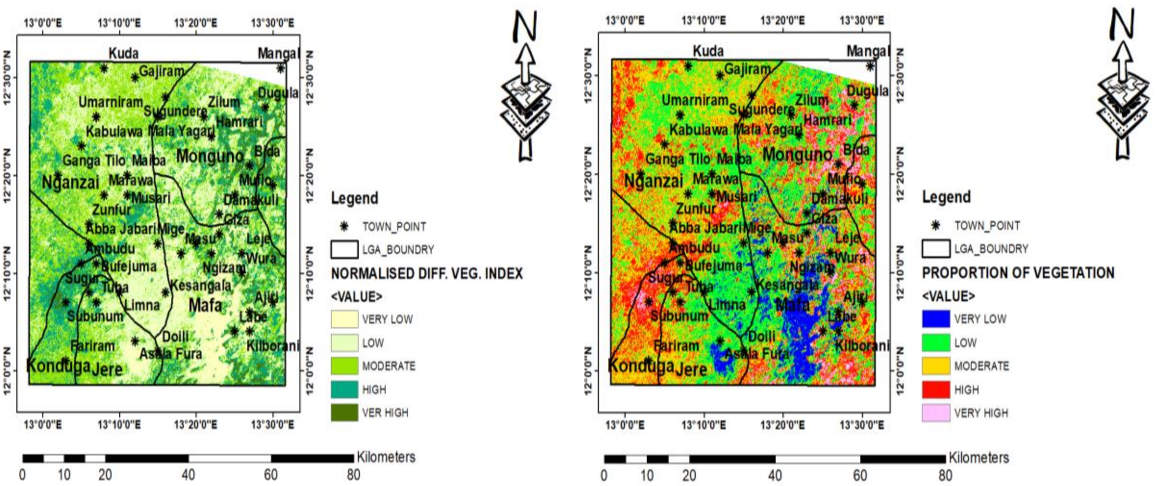

(c) (d)

Figure 10: (c) NDVI, (d) Proportion of Veg Map of the study area

4. Discussion of results

The assessment of geothermal renewable energy potential of the Chad Basin using combined Aeroradiometric and remote sensing techniques has provided a robust framework for delineating high-potential geothermal zones. The integration of these two approaches demonstrates a consistent spatial pattern of geothermal anomalies, with results strongly supported by subsurface bottom-hole temperature (BHT) evidence from drilled wells. The Aeroradiometric dataset highlights significant variations in the distribution of radioactive heat-producing elements across the study area. Total count radiation (Figure 3), uranium (Figure 6), thorium (Figure 4), and potassium (K^{40}) (Figure 5) maps reveal a dominant northwest–southeast trend, with high concentrations localized in the southeastern to central corridor (12°00'–12°15'N, 13°05'–13°25'E).

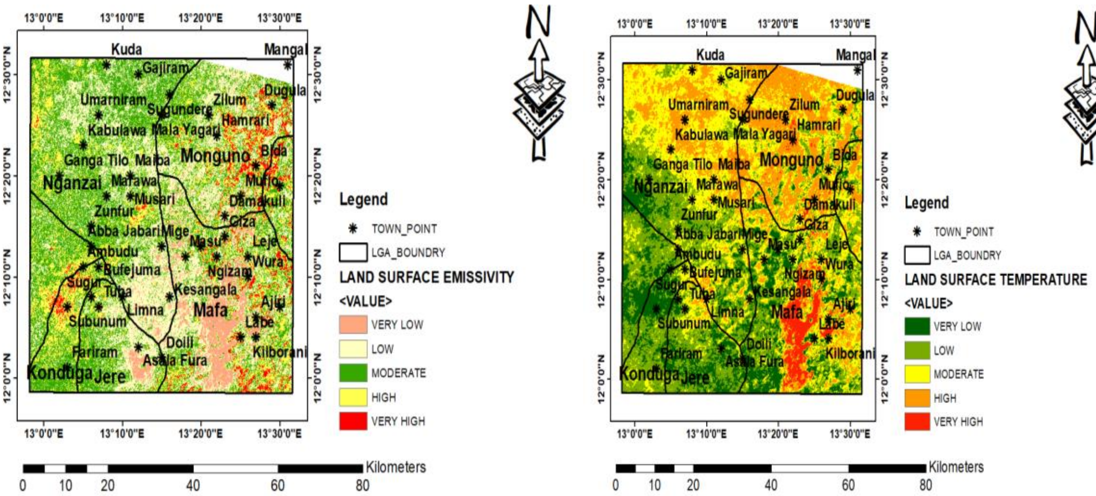

(e) (f)

Figure 10: (e) Land Surface Emissivity and (f) Land Surface Temperature Map of the study area

The ternary radiometric map (Figure 7) indicates felsic basement lithologies enriched in U, Th, and K^{40}, while radiogenic heat production (RHP) estimates (Figure 8) reach values as high as 53.1 μW/m³. These values are significantly higher than the 0.17–1.90 μW/m³ previously documented by Ali and Orazulike, 201 for sedimentary sections, pointing to the role of crystalline basement intrusions in driving heat anomalies.

The remote sensing results corroborate the Aeroradiometric findings. Lineament analysis (Figures 9a–b) reveals NE–SW and NW–SE fault systems that enhance crustal permeability and fluid migration. Hydrothermal alteration zones (Figure 9c) mapped in Mafa, Asula Fura, and Kesangala coincide spatially with Aeroradiometric anomalies, suggesting active geothermal processes. Land surface temperature (LST) anomalies (Figure 10f) are most pronounced in Kilborani, Ajiri, and Mafa, aligning with structurally controlled corridors of alteration. Variations in emissivity and vegetation indices (Figures 10c–e), further confirm thermal heterogeneity in the southeastern sector, reflecting shallow heat sources and enhanced geothermal activity.

When integrated with subsurface data, these results demonstrate remarkable consistency. Tyoh et al. (2021) reported corrected geothermal gradients of ~37.5 °C/km and heat flow values between 63–95 mW/m² in the Bornu Basin, while a broader analysis of 14 wells revealed average heat flow of ~80.6 mW/m² across the Chad Basin (DOAJ, 2022). Lawal et al. (2017) estimated Curie point depths of 18–25 km with corresponding heat flow values of 60–85 mW/m², further confirming elevated geothermal gradients. Earlier works by Ofoegbu (1984), Avbovbo et al. (1986), and Obaje (2009) had also emphasized the influence of magmatism and structural deformation on the basin's thermal regime. The high RHP values (>20 μW/m³), shallow Curie depths, elevated BHT, and high LST anomalies observed in this study collectively identify the southeastern Chad Basin (Mafa–Ajiri–Asula Fura corridor) as the most prospective zone for geothermal renewable energy exploration. In contrast, the northwestern sector (Nganzai–Monguno) exhibits low RHP (<10 μW/m³), weak alteration, subdued LST anomalies, and thick sedimentary cover. These features correspond to low geothermal gradients and reduced BHT values, indicating poor geothermal potential in that zone.

This integrated analysis underscores the importance of combining Aeroradiometric and remote sensing datasets with well data in geothermal assessments. The strong correlation between surface radiometric anomalies, remote sensing indicators, and subsurface BHT validates the southeastern Chad Basin as a geothermal hotspot. These findings align with global intraplate rift basin studies, which highlight the interplay of crustal deformation, radiogenic enrichment, and magmatic intrusions in elevating geothermal gradients (Fairhead, 1986). Consequently, this work contributes not only to local energy prospectively but also to the broader understanding of geothermal systems in sedimentary rift basins.

5. Conclusion

This study demonstrates the effectiveness of integrating Aeroradiometric and remote sensing techniques for geothermal resource assessment of the Chad Basin, northeast Nigeria. Aeroradiometric analysis reveals that uranium, thorium, and potassium (K^{40}) anomalies are strongly concentrated in the southeastern sector, where radiogenic heat production values exceed 50 μW/m³. Remote sensing interpretation highlights structurally controlled corridors of lineament density, hydrothermal alteration zones, and elevated LST anomalies, all of which align spatially with high RHP regions.

When compared with previous geothermal studies, including BHT-derived gradients (~37.5 °C/km), Curie point depths (18–25 km), and measured heat flow (63–95 mW/m²), the integrated results confirm that the southeastern Chad Basin is the most prospective zone for geothermal development. The coincidence of radiogenic enrichment, structural permeability, and thermal anomalies underscores the role of basement intrusions and tectonic structures in localizing geothermal systems.

The findings of this study not only advance the understanding of geothermal energy potential of the Chad Basin but also provide a methodological framework for renewable energy exploration in other frontier basins of Africa. Further detailed geophysical surveys, coupled with exploratory drilling, are recommended to validate the identified anomalies and advance geothermal resource development in the region.

References

Abdullahi, U. G., Lawal, T. O., and Yakubu, T. A. (2022). Heat flow and geothermal gradient estimation from spectral analysis of aeromagnetic data over part of the Chad Basin, Nigeria. *Journal of African Earth Sciences, 193,* 104545. https://doi.org/10.1016/j.jafrearsci.2022.104545

Ali, M. I., and Orazulike, D. M. (2010). Radiogenic heat production in rocks of the Nigerian sector of the Chad Basin, *Global Journal of Geological Sciences, 8*(1), 1–10.

Avbovbo, A. A., Ayoola, E. O., and Osahon, G. A. (1986). Depositional and structural styles in Chad Basin of northeastern Nigeria, *AAPG Bulletin, 70*(12), 1787–1798.

Barber, W. (1965). Pressure water in the Chad Formation of Bornu and Dikwa Emirates, North-East Nigeria, *Geological Survey of Nigeria Bulletin, 35,* 1–138.

Bertani, R. (2016). Geothermal power generation in the world 2010–2014 update report, *Geothermics, 60,* 31–43. https://doi.org/10.1016/j.geothermics.2015.11.003

Carter, J. D., Barber, W., Tait, E. A., and Jones, G. P. (1963). *The geology of parts of Adamawa, Bauchi and Borno Provinces in North-Eastern Nigeria,* Geological Survey of Nigeria Bulletin, No. 30.

DiPippo, R. (2021). *Geothermal power plants: Principles, applications, case studies, and environmental impact* (5th ed.), Butterworth-Heineman, Elsevier book aid international. 253 – pages.

DOAJ. (2022). Heat flow estimates from oil wells in the Nigerian sector of the Chad Basin, *Journal of Geothermal Studies, 14*(2), 45–59.

Egwumah, F. A., Okwoli, E., and Abubakar, M. B. (2020). Renewable energy development in Nigeria: Status, challenges, and prospects, *Energy Reports, 6,* 993–1004. https://doi.org/10.1016/j.egyr.2020.11.013

Fairhead, J. D. (1986). Geophysical controls on sedimentation within continental rifts. In P. L. Hancock (Ed.), *Sedimentation in continental rifts* (pp. 19–27), Geological Society, London, Special Publications.

Jiménez-Muñoz, J. C., Cristóbal, J., Sobrino, J. A., Soria, G., Ninyerola, M., and Pons, X. (2014). Revision of the single-channel algorithm for land surface temperature retrieval from Landsat thermal-infrared data, *IEEE Transactions on Geoscience and Remote Sensing, 52*(2), 839–853. https://doi.org/10.1109/TGRS.2013.2244536

Lawal, T. O., Olasehinde, P. I., and Olatinwo, M. O. (2017). Evaluation of depth to the bottom of magnetic sources and heat flow from high-resolution aeromagnetic data of part of Nigeria sector of Chad Basin, *Arabian Journal of Geosciences, 10*(19), 421. https://doi.org/10.1007/s12517-017-3211-2

[13] Lawal, T. O., Onwuemesi, A. G., Anakwuba, E. K., Chinwuko, A. I., and Usman, A. O. (2017). Evaluation of the depth to the bottom of magnetic sources and heat flow from high-resolution aeromagnetic data of part of the Nigeria sector of the Chad Basin, *Arabian Journal of Geosciences, 10*(17), 389. https://doi.org/10.1007/s12517-017-3186-3

Ngah, S. A., and Abubakar, M. B. (2018). Hydrogeological significance of Chad Formation in Borno State, Northeastern Nigeria, *Journal of African Earth Sciences, 143,* 120–132.

Nwankwo, C. N. (2021). A review of geothermal energy research and development in Nigeria, *Renewable and Sustainable Energy Reviews, 143,* 110903. https://doi.org/10.1016/j.rser.2021.110903

Obaje, N. G. (2009). *Geology and mineral resources of Nigeria,* Springer, Nature – 221 pages.

Ofoegbu, C. O. (1984). Interpretation of aeromagnetic anomalies over the Lower and Middle Benue Trough of Nigeria, *Geophysics, 49*(2), 178–185.

Offodile, M. E. (1992). *An approach to groundwater study and development in Nigeria,* Mecon Geology and Engineering Services Ltd.

Pour, A. B., and Hashim, M. (2015). Structural mapping using PALSAR data in the Central Gold Belt, Malaysia, *Ore Geology Reviews, 64,* 13–22. https://doi.org/10.1016/j.oregeorev.2014.06.011

Rybach, L. (1988). Determination of heat production rate. In R. Haenel, L. Rybach, and L. Stegena (Eds.), *Handbook of terrestrial heat-flow density determination* (pp. 125–142). Springer.

Sobrino, J. A., Jiménez-Muñoz, J. C., and Paolini, L. (2004). Land surface temperature retrieval from Landsat TM 5, *Remote Sensing of Environment, 90*(4), 434–440. https://doi.org/10.1016/j.rse.2004.02.003

Tyoh, B. F., Tse, A. C., and Pam, R. I. (2021). Estimation of heat flow and geothermal gradient from bottom-hole temperature data of the Bornu Basin, Nigeria, *Journal of African Earth Sciences, 181,* 104234. https://doi.org/10.1016/j.jafrearsci.2021.104234

Tyoh, T. A., Onwuemesi, A. G., Anakwuba, E. K., Chinwuko, A. I., and Usman, A. O. (2021). Geothermal gradient and heat flow estimates from bottom hole temperature data of Bornu Basin, Chad Basin, Nigeria, *Applied Geophysics, 18*(1), 23–36.

USGS. (2019). *Landsat 8 (L8) data users handbook* (Version 5.0), U.S. Geological Survey.

Wubalem, A., and Solomon, K. (2023). Remote sensing applications in geothermal exploration: A review, *Geosciences, 13*(2), 71 – 90. https://doi.org/10.3390/geosciences13020071

Yalcin, T. (2021). Integration of remote sensing and GIS techniques for geothermal resource exploration, *Geothermics, 90,* 101993. https://doi.org/10.1016/j.geothermics.2020.101993